Subsurface structure of a buried Eratosthenian crater on the far-side of the Moon

Ling Zhang [a], Chunyang Zhao [a], Xintong Dong [b,*], Shaoping Lu [a], Yi Xu [c], Yuqi Qian [d], Shuo Han [a], Zhijun Huo [a], Rui Gao [a]

[a] *School of Earth Science and Geological Engineering, Sun Yat-sen University, Guangzhou, China*
[b] *College of Instrumentation and Electrical Engineering, Jilin University, Changchun, China*
[c] *State Key Laboratory of Lunar and Planetary Sciences, Macau University of Science and Technology, Macau, China*
[d] *Department of Earth Sciences and Laboratory for Space Research, The University of Hong Kong, Hong Kong, China*

ABSTRACT

Impact craters represent the most prominent geological features on the Moon. Current methodologies for investigating impact craters primarily involve morphological analysis and numerical simulations. However, direct subsurface structural data of lunar impact craters remain scarce. Utilizing the Lunar Penetrating Radar (LPR) aboard the Yutu-2 rover, we conducted comprehensive subsurface exploration of the Chang'e-4 landing area on the lunar far-side over 65 lunar days, acquiring unprecedented dual-channel radar profiles of a buried Eratosthenian crater, characterized by a rim-to-floor diameter of 484 m and subsurface structural features extending to 215 m depth. Our comprehensive analysis delineates a 12-layer stratigraphic architecture comprising lunar regolith, paleoregolith horizons, ejecta deposits, and basalt units, while simultaneously reveals characteristic subsurface features of lunar impact structures, including reworked zones, radial collapses, central rebounds, and fracture systems. These findings establish a critical foundation for understanding crater formation mechanisms from surface expressions to subsurface responses, while providing new constraints on the impact chronology and origin of impactors within the South Pole-Aitken (SPA) basin.

1. Introduction

Impact craters represent ubiquitous geological markers across all solid bodies within the solar system, preserving the enduring imprint of the solar system's collisional past. Their morphological characteristics encode vital information about impactor parameters (mass, velocity, incidence angle) and target body properties (density, structural heterogeneity) (Kenkmann et al., 2014). However, the dynamic evolution of planetary surfaces has obscured many primordial crater records through erosional processes, tectonic activities, and sedimentary infilling (Davison and Collins, 2022). Terrestrial crater preservation exemplifies this geological filtering - despite Earth's active surface processes, merely ~200 confirmed impact structures persist (Nicholson et al., 2022). In contrast, the Moon's quiescent geological environment, devoid of atmospheric weathering and plate tectonics, preserves impact features with exceptional fidelity, retaining craters dating back to the Late Heavy Bombardment epoch (~4 Ga) (Moriarty and Pieters, 2018). This pristine crater inventory provides unparalleled insights into solar system

evolution and planetary surface processes (Racki and Koeberl, 2024).

As the most crater-dense planetary body, the Moon hosts the South Pole-Aitken (SPA) basin - a superlative impact structure spanning 2500 km in diameter and resulting a ~13 km depression depth (Huang et al., 2020). This ancient basin, encompassing nearly a quarter of the lunar nearside, preserves critical evidence of early solar system impactor flux and lunar differentiation processes. Contemporary crater studies employ three principal methodologies: 1) multispectral remote sensing (visible, infrared, radar) for surface composition and morphology analysis (Hiesinger et al., 2012; Moriarty and Pieters, 2018), 2) numerical modeling of impact dynamics and crustal response (Collins, 2014), and 3) experimental simulations replicating hypervelocity impacts (Halim et al., 2021). While these approaches elucidate surface manifestations, they remain limited in characterizing subsurface structural modifications induced by impact events.

To address this knowledge gap, China's Chang'e-4 mission targeted the Von Kármán crater within the SPA basin - a strategic location for investigating primordial lunar crustal materials (Wu et al., 2019; Fig. 1).

The SPA basin's formation during the Moon's early differentiation phase (~4 Ga) makes it a unique window into both lunar accretionary processes and early solar system impact chronology (Huang et al., 2018). The mission's Yutu-2 rover deployed dual-frequency Lunar Penetrating Radar (LPR) to probe subsurface stratigraphy, utilizing 60 MHz (low-frequency) and 500 MHz (high-frequency) channels for deep and shallow investigations respectively (Li et al., 2020).

The low-frequency radar revealed a 360-meter stratified sequence comprising multiple magma flow units (Zhang J. et al. 2021; Lai et al. 2020; Zhang et al. 2020; Yuan et al. 2021), while high-frequency data resolved three distinct regolith layers: surface-weathered material overlying alternating coarse/fine ejecta deposits (Li et al., 2020; Zhou et al., 2022). Subsequent dielectric and mineralogical analyses of these layers have advanced our understanding of regolith maturation processes and impact-induced mechanical alterations (Ding et al., 2021; Giannakis et al., 2024; Feng et al. 2022).

Extended rover operations over 65 lunar days have yielded groundbreaking discoveries: a buried Eratosthenian-age crater exhibiting 200-meter vertical penetration through multiple stratigraphic units. This structure displays characteristic impact deformation features including central uplift, radial fracture systems, and reworked zones - providing the first in situ evidence of subsurface crater modification processes. These findings fundamentally enhance our capacity to interpret impact crater subsurface architecture and associated energy dissipation mechanisms.

2. Regional geological context

To investigate the geological evolution of the Chang'e-4 landing zone, we have systematically identified and chronologically ordered the major geological events that have shaped the study area (Fig. 1). The geological history began with the formation of the South Pole-Aitken (SPA) basin during the Pre-Nectarian period (>3.92 Ga). This was followed by the formation of the Von Kármán crater (~3.9 Ga) during the Nectarian period (Stuart-Alexander, 1978). The subsequent impact that formed the Leibniz crater to the north (Yingst et al., 2017) significantly altered the Von Kármán crater through ejecta deposition and structural modification. During the Late Imbrian period, the region experienced multiple phases of basaltic volcanism (Pasckert et al., 2018), which progressively filled the Von Kármán crater with mare deposits. The early stages of this volcanic activity coincided with the formation of the Alder crater southeast of Von Kármán (Pasckert et al., 2018). As volcanic activity continued, two smaller impact craters formed: the Von Kármán L' crater during the main phase of basalt emplacement, followed by the Von Kármán L crater in the terminal stages of volcanic activity (Fu et al., 2020). The most recent significant geological event was the formation of the Finsen crater during the early Eratosthenian period (Ling et al., 2019). This impact event deposited ejecta across the landing area, which now constitutes the primary component of the lunar regolith. Following this event, the region entered an extended period of geological quiescence, during which the surface materials underwent continuous space weathering through micrometeorite bombardment and solar wind irradiation.

3. Results

3.1. LPR data processing

After 65 lunar days of operation, the Yutu-2 rover traversed approximately 1600 m (Fig. 2), with the LPR continuously collecting data along its path. The radar data underwent the following processing sequence:

1. Data format conversion: The CE-4 LPR data, conforming to the Planetary Data System (PDS) standard format, were converted
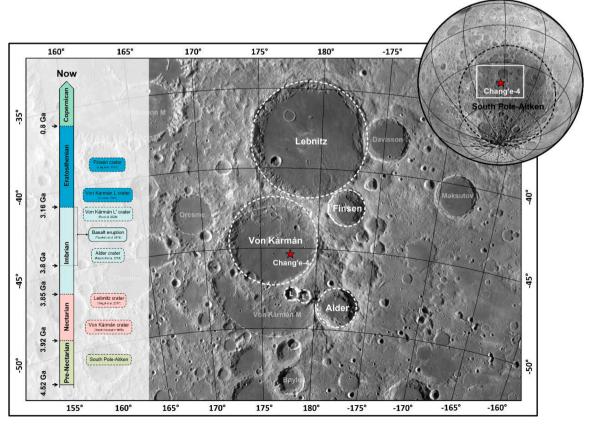

Fig. 1. Landing zone of the Chang'e-4 mission and Chronological sequence of major geological events shaping the area.
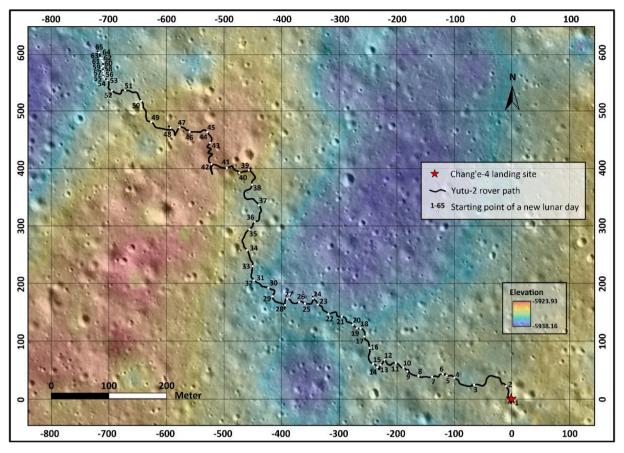
Fig. 2. Path of Yutu-2 during 65 lunar days (2019.1.4–2024.03.15). The base image is the LROC NAC image (M1303619844LR), and the DEM established by the image pairs (M1303619844LR and M1303640934LR).

from raw data into binary format for subsequent processing and analysis.

2. Data concatenation: As data from different lunar days were stored separately, individual files were sequentially read and concatenated to form complete radar profiles.

3. Redundant trace removal: During stationary periods when the rover conducted other measurements, the LPR continued data acquisition, resulting in duplicate traces at specific locations, which were subsequently removed.

4. Timing correction: The receiving antennas activated 28.203 ns (high-frequency channel) and 70 ns (low-frequency channel) prior to the transmitting antenna. These premature signals were eliminated through temporal adjustment.

5. Background noise suppression: Surface reflections and lateral noise were mitigated by subtracting the average trace from the dataset.

6. Bandpass filtering: The bandpass filter cutoff frequencies were carefully configured based on each antenna channel's operational bandwidth (Jia et al., 2018). For the high-frequency channel (250–750 MHz), the parameters were set at 150 MHz (stopband upper limit), 250 MHz (passband lower limit), 750 MHz (passband upper limit), and 850 MHz (stopband lower limit). Similarly, the low-frequency channel (30–90 MHz) used cutoff values of 20 MHz, 30 MHz, 90 MHz, and 100 MHz for the corresponding frequency bands, ensuring optimal signal preservation while effectively removing out-of-band noise.

7. Signal gain application: To compensate for signal attenuation with depth, gain functions were implemented to enhance deeper reflections.

8. Median filtering: Residual Gaussian noise, particularly in deeper sections, was reduced through median filtering to improve profile clarity.

9. Channel balancing: Horizontal amplitude inconsistencies resulting from background removal were corrected through inter-channel balancing.

10. Spatial interpolation: Irregular sampling intervals along the traverse were normalized through nearest neighbor spatial interpolation.

11. Migration processing: Frequency-wavenumber (f-k) migration was performed with $\varepsilon_r = 5$ for accurate imaging, after evaluating constrained values reported by previous studies (Zhang J. et al., 2021; Lai et al., 2020).

12. Signal enhancement: Field training and validation datasets generated by robust principal component analysis are fed into a multi-scale attention convolutional neural network (Dong et al., 2022), and we use the well-trained model to enhance the desired signals.

Following this comprehensive processing sequence, high-resolution profiles from both frequency channels were obtained, enabling clear imaging from shallow to deep subsurface structures (Figs. 3 and 4).

3.2. Stratigraphic sequence

The dual-frequency LPR provides complementary subsurface characterization, with high-frequency data offering fine-scale resolution of shallow structures and low-frequency data revealing deeper stratigraphic features. The LPR's vertical resolution is approximately 0.17 m for the high-frequency channel and 2.8 m for the low-frequency channel
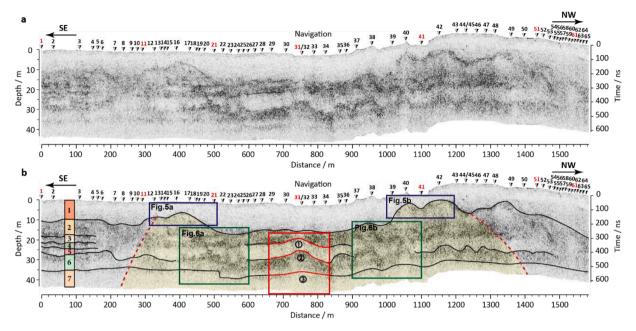
Fig. 3. High-frequency radar profile from LPR over 65 lunar days. (a) High-frequency radar profile. (b) Geological interpretation of radar profile with stratigraphic analysis. The left panel of (b) presents a detailed stratigraphic column showing seven distinct layers within the upper 40 m: (1) lunar regolith layer; (2–6) interbedded sequence of paleoregolith, basalt flows, and ejecta deposits; and (7) basaltic bedrock. The yellow highlighted region reveals the upper section of a buried paleo-impact crater, displaying characteristic morphological features including central rebound (red box), radial collapse (green box), and reworked zone (blue box). The high-resolution data obtained from the second channel are presented in the Appendix for detailed reference.

(Zhang et al. 2014), while horizontal resolution is approximately 0.037 m for the high-frequency channel and 0.16 m for the low-frequency channel depending on along track sampling interval. These resolution characteristics directly influence our ability to detect subsurface features, with fractures and layers requiring widths exceeding 0.17 m (high-frequency) or 2.8 m (low-frequency) for reliable identification. Integration of 65 lunar days' radar observations with previous findings (Zhang J. et al., 2021; Lai et al., 2020; Zhang et al., 2020; Yuan et al., 2021) has enabled the construction of a comprehensive stratigraphic column:

1. Lunar Regolith Layer: The high-frequency radar data reveal a ~10 m thick regolith layer, extensively characterized as Finsen crater ejecta deposits subjected to billions of years of space weathering.

2. Paleo-regolith Layer: Morphological analysis of buried craters suggests the presence of a flat-bottomed impact structure, indicative of a dual-layer system comprising a competent basaltic basement overlain by unconsolidated paleo-regolith (Zhang et al., 2025).

3. Thin Basalt Layer: A distinct, laterally continuous reflector interpreted as a primary basalt flow unit.

4. Transitional Layer: Either thin basalt flows or ejecta deposits, showing intermediate radar characteristics.

5. Basalt Layer: A prominent, ~10 m thick radar unit exhibiting minimal signal scattering, interpreted as a massive basalt flow prior to subsequent impact disruption.

6. Paleo-regolith Layer: Secondary regolith development between major basalt units.

7. Basalt Bedrock: The deepest detectable unit in high-frequency data, representing competent basement material.

8. Stratified Layer: Low-frequency data reveal finely layered sequences, potentially representing either multiple thin basalt flows or stratified ejecta deposits.

9. Basalt Layer: A major volcanic unit identified in the low-frequency radar profile.

10. Ejecta Layer: Morphological and stratigraphic relationships suggest derivation from the Schrödinger impact event (Cao et al., 2023).

11–12. Basalt Layers: Deep-seated volcanic units separated by paleo-regolith, indicative of significant eruptive episodes.

3.3. Buried crater characteristics

The radar profiles reveal the complete subsurface structure of a buried impact crater, providing unprecedented insights into its structural features. The high-resolution data (Fig. 3) clearly display several diagnostic characteristics of the impact structure:

1. **Reworked zone** (Fig. 5): The initial impact created symmetric ejecta deposits along the crater walls, forming a distinct zone of reworked materials characterized by radar reflectors.

2. **Radial Collapse** (Fig. 6): Post-impact gravitational adjustment generated characteristic radial collapse features beneath the crater floor, clearly visible in high-frequency radar data as divergent linear reflectors.

3. **Central Rebound** (red box in Figs. 3 and 4): The medium-sized impact crater exhibits a transitional morphology between simple and complex craters, with stress rebound creating a distinct central uplift rather than a well-developed peak ring. This feature provides crucial information about the impact energy and target material properties.

4. **Fracture Zone** (base of the impact response zone in Fig. 4): The impact-generated stress field produced extensive fracturing, particularly along lithological interfaces. The fracture density decreases with depth.

These features collectively provide a comprehensive understanding of the impact process, from initial crater formation to subsequent structural modification. The preservation of these subsurface features offers valuable insights into the mechanical properties of lunar materials and the energy dynamics of medium-sized impacts.
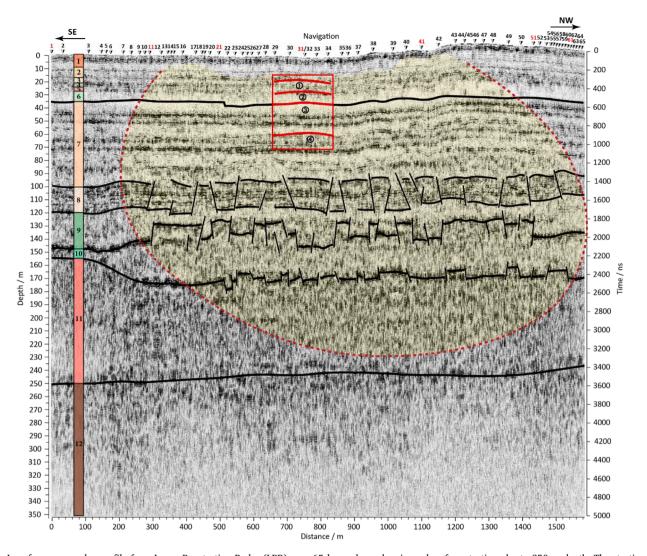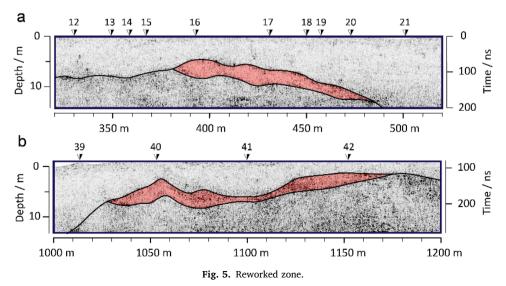
Fig. 4. Low-frequency radar profile from Lunar Penetrating Radar (LPR) over 65 lunar days, showing subsurface stratigraphy to 350 m depth. The stratigraphic column on the left delineates twelve distinct layers: Layers 1–7 correspond to the shallow stratigraphy identified in Fig. 3; Layer 8 comprises either ejecta deposits or multiple thin basalt flows; Layer 9 represents a continuous basalt unit; Layer 10 consists of ejecta material from the Schrödinger impact event. Layers 11 and 12 are thick basaltic units separated by paleo-regolith, indicative of significant eruptive episodes. The yellow highlighted region reveals the complete subsurface architecture of a buried paleo-impact crater, displaying characteristic structural features including central uplift (red box) and associated fault systems at the crater base. The high-resolution data obtained from the first channel are presented in the Appendix for detailed reference.
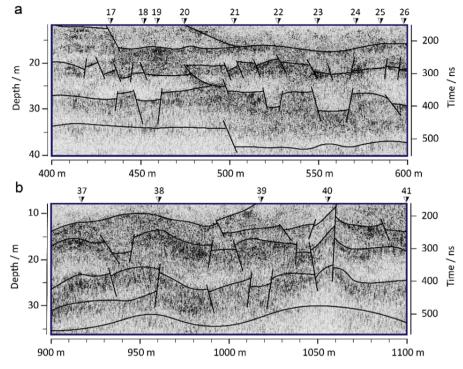

Fig. 5. Reworked zone.

Fig. 6. Radial collapse.

4. Discussion

4.1. Three-dimensional structure and morphometric parameters of the crater

Based on the spatial distribution of radar data, we reconstructed the three-dimensional structure of the impact crater (Fig. 7). The model reveals several key morphometric parameters: the crater diameter (D_C = 484 m), the lateral extent of the impact-affected zone (D_X = 824 m), and the vertical depth of the response zone (D_Y = 215 m). The dimensional ratios of these features are consistent with those of typical lunar impact craters (Pierazzo and Melosh, 2000), supporting the interpretation of its impact origin.

The buried crater exhibits morphological characteristics consistent with a flat-bottomed impact structure (Zhang et al., 2025), having formed within an ancient, unconsolidated lunar regolith unit that was subsequently mantled by ejecta deposits from Finsen crater. Morphometric analysis of such features typically focuses on three fundamental parameters: (1) crater rim diameter (D_A), (2) basal floor diameter (D_F), and (3) overlying regolith thickness (t). While the observed D_F/D_A ratio of 0.6 falls within the empirically derived range of 0.2–0.7 for flat-bottomed craters (Quaide and Oberbeck, 1968), the measured D_A/t
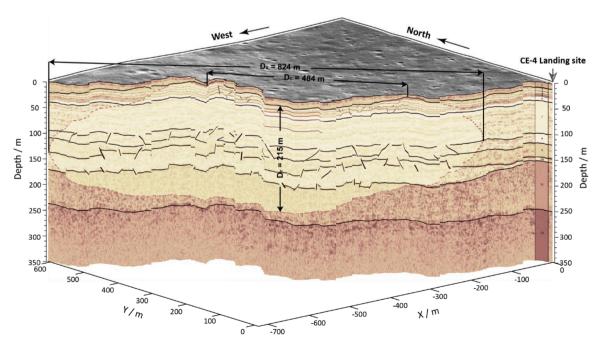

Fig. 7. Comprehensive interpretation of the 3D crater structure.

ratio demonstrates significant deviation from predicted values, suggesting substantial post-formational modification. This anomaly is further supported by the crater's markedly reduced flank slopes (10.6° and 9.3° for left and right walls respectively), which contrast sharply with the characteristic ~31° slopes observed in pristine lunar impact craters. Collectively, these morphometric discrepancies strongly indicate that the structure has undergone extensive degradation, likely through prolonged surface processes including regolith gardening and mass wasting.

4.2. Formation age: early to mid-Eratosthenian period

The stratigraphic relationships constrain the formation age of the crater. As shown in Fig. 2, the crater is buried beneath the first regolith layer, which is widely attributed to ejecta from the Finsen crater, dated to the Eratosthenian period (Ling et al., 2019). This provides a lower age limit for the studied crater. Additionally, the crater postdates the major phase of lava flooding in Mare Imbrium, placing its upper age limit in the early Eratosthenian. Morphological analysis of the crater, including wall slope degradation, suggests it underwent approximately 1 Ga of surface weathering before burial (Zhang et al., 2025). These constraints indicate the crater formed during the early to mid-Eratosthenian period.

4.3. Oblique impact from the southeast

The observed subsurface deformation patterns may suggest an impact trajectory from generally southeast directions, though the 2D imaging constraints prevent unambiguous azimuthal determination:

1. **Central Uplift Structure**: The asymmetric distribution of the four central uplift peaks (red boxes in Figs. 3 and 4) shows an elongation from the upper left to lower right, consistent with a southeast-directed impact.
2. **Impact Zone Geometry**: The asymmetric shape of the impact-affected zone (yellow area in Fig. 4) further supports a southeast impact trajectory.
3. **Ejecta Distribution**: The reworked zone (blue box in Fig. 3) exhibits uneven ejecta accumulation, with greater thickness and elevation on the right side, indicative of an oblique impact from the southeast.

A series of oblique impact simulations on the Moon and other planetary bodies have been conducted by previous researchers (Davison and Collins, 2022; Pierazzo and Melosh, 2000). Based on surface morphology modeling (Davison and Collins, 2022), the buried crater (Fig. 3) in this study shows similarities to those formed by low-angle oblique impacts—where "low-angle" refers to a shallow impact angle relative to the vertical—even though the crater has undergone some degree of degradation. Subsurface structural effects (Fig. 3; Pierazzo and Melosh, 2000) further support this interpretation, as the deformation pattern also closely resembles those resulting from low-angle oblique impacts.

4.4. Comparison with terrestrial impact craters

A recent discovery of a complex crater on the Guinea Plateau, West Africa, provides an interesting terrestrial analog (Nicholson et al., 2022), with a diameter of ~8–9 km and Late Cretaceous formation age (~66 Ma). Both craters exhibit similar features, including central uplift (prominent peak on Earth, subtle rebound on the Moon), radial collapse structures, and extensive subsurface deformation. However, differences arise from their target materials: the lunar crater formed in a weathered regolith layer, while the terrestrial crater involved water-rich sediments that attenuated impact energy. These comparisons highlight the potential for discovering more buried craters on terrestrial planets and their implications for planetary evolution.

5. Conclusion

The Yutu-2 rover's continuous acquisition of high-frequency and low-frequency radar data has revealed a newly discovered buried crater dating to the Eratosthenian period. This ancient impact structure penetrates multiple geological layers, with a response depth exceeding 200 m The crater exhibits well-preserved subsurface features, including reworked zones, radial collapse structures, central uplift, and fracture zones, providing unprecedented insights into the subsurface characteristics of lunar impact craters. Morphological analysis confirms an oblique impact from the southeast direction. It should be noted that impact direction inferences from single-profile LPR data contain inherent uncertainties. Comparisons with terrestrial analogs reveal both similarities and unique aspects of lunar impact processes. These findings provide critical evidence for understanding the surface-to-interior structure of lunar craters and their formation mechanisms.

CRediT authorship contribution statement

Ling Zhang: Writing – original draft, Visualization, Methodology, Conceptualization. **Chunyang Zhao:** Investigation, Formal analysis. **Xintong Dong:** Writing – review & editing, Supervision, Methodology. **Shaoping Lu:** Writing – review & editing, Supervision, Project administration. **Yi Xu:** Funding acquisition, Conceptualization. **Yuqi Qian:** Investigation, Conceptualization. **Shuo Han:** Visualization, Investigation. **Zhijun Huo:** Methodology. **Rui Gao:** Supervision.

Declaration of competing interest

We declare that we have no financial and personal relationships with other people or organizations that could inappropriately influence our work, there is no professional or other personal interest of any nature or kind in any product, service and/or company that could be construed as influencing the position presented in, or the review of, the manuscript entitled.

Acknowledgements

Supplementary materials

Supplementary material associated with this article can be found, in the online version, at doi:10.1016/j.epsl.2025.119542.

Data availability

Data will be made available on request.

References

Cao, H., Xu, Y., Xu, L., Zhang, L., Bugiolacchi, R., Zhang, F., 2023. From Schrödinger to Von Kármán: an intriguing new geological structure revealed by the Chang'e-4 lunar penetrating radar. Geophys. Res. Lett. 50 (2), e2022GL101413. https://doi.org/10.1029/2022GL101413.

Collins, G.S., 2014. Numerical simulations of impact crater formation with dilatancy. J. Geophys. Res.: Planets 119 (12), 2600–2619. https://doi.org/10.1002/2014JE004708.

Davison, T.M., Collins, G.S., 2022. Complex crater formation by oblique impacts on the Earth and Moon. Geophys. Res. Lett. 49 (15), e2022GL101117. https://doi.org/10.1029/2022GL101117.

Ding, C., Xiao, Z., Wu, B., Li, Z., Su, Y., Zhou, B., et al., 2021. Rock fragments in shallow lunar regolith: constraints by the lunar penetrating radar onboard the Chang'E-4 mission. J. Geophys. Res.: Planets 126 (8), e2021JE006917. https://doi.org/10.1029/2021JE006917.

Dong, X.T., Lin, J., Lu, S.P., Wang, H.Z., Li, Y., 2022. Multiscale spatial attention network for seismic data denoising. IEEE Trans. Geosci. Remote Sens. 60, 5915817. https://doi.org/10.1109/TGRS.2022.3145915.

Feng, J., Siegler, M.A., White, M.N., 2022. Dielectric properties and stratigraphy of regolith in the lunar South Pole-Aitken basin: observations from the Lunar Penetrating Radar. Astron. Astrophys. 661, A47. https://doi.org/10.1051/0004-6361/202143015.

Fu, X., Qiao, L., Zhang, J., et al., 2020. The subsurface structure and stratigraphy of the Chang'E-4 landing site: orbital evidence from small craters on the Von Kármán crater floor. Res. Astron. Astrophys. 20 (1), 1. https://doi.org/10.1088/1674-4527/20/1/8.

Giannakis, I., McDonald, C., Feng, J., et al., 2024. Automatic segmentation of radar data from the Chang'E-4 mission using unsupervised machine learning: a data-driven interpretation approach. Icarus 417, 116108. https://doi.org/10.1016/j.icarus.2024.116108.

Halim, S., Koeberl, C., Ferrière, L., 2021. Numerical modeling of the formation of Shackleton crater at the lunar south pole. Icarus 354, 113992. https://doi.org/10.1016/j.icarus.2020.113992.

Hiesinger, H., van der Bogert, C.H., Pasckert, J.H., et al., 2012. How old are young lunar craters? J. Geophys. Res.: Planets 117 (E12). https://doi.org/10.1029/2011JE003935.

Huang, J., Xiao, Z., Flahaut, J., Martinot, M., Head, J., Xiao, X., et al., 2018. Geological characteristics of Von Kármán crater, northwestern South Pole-Aitken Basin: chang'E-4 landing site region. J. Geophys. Res.: Planets 123 (7), 1684–1700. https://doi.org/10.1029/2018JE005577.

Huang, J., Xiao, Z., Flahaut, J., et al., 2020. Diverse rock types detected in the lunar South Pole–Aitken Basin by the Chang'E-4 lunar mission. Geology 48 (8), 723–727. https://doi.org/10.1130/G47280.1.

Jia, Y., Zou, Y., Ping, J., Xue, C., Yan, J., Ning, Y., 2018. The scientific objectives and payloads of Chang'E-4 mission. Planet. Space Sci. 162, 207–215. https://doi.org/10.1016/j.pss.2018.02.011.

Kenkmann, T., Poelchau, M.H., Wulf, G., 2014. Structural geology of impact craters. J. Struct. Geol. 62, 156–182. https://doi.org/10.1016/j.jsg.2014.01.015.

Lai, J., Xu, Y., Bugiolacchi, R., et al., 2020. First look by the Yutu-2 rover at the deep subsurface structure at the lunar farside. Nat. Commun. 11, 3426. https://doi.org/10.1038/s41467-020-17262-w.

Li, C., Su, Y., Pettinelli, E., et al., 2020. The Moon's farside shallow subsurface structure unveiled by Chang'E-4 lunar Penetrating radar. Sci. Adv. 6 (36), eaay6898. https://doi.org/10.1126/sciadv.aay6898.

Ling, Z., Qiao, L., Liu, C., Cao, H., Bi, X., Lu, X., et al., 2019. Composition, mineralogy and chronology of mare basalts and non-mare materials in Von Kármán crater: landing site of the Chang'E-4 mission. Planet. Space Sci. 179, 104741. https://doi.org/10.1016/j.pss.2019.104741.

Moriarty III, D.P., Pieters, C.M, 2018. The character of South Pole-Aitken Basin: patterns of surface and subsurface composition. J. Geophys. Res.: Planets 123 (3), 729–747. https://doi.org/10.1002/2017JE005364.

Nicholson, U., Bray, V.J., Gulick, S.P., Aduomahor, B., Morgan, J.V., 2022. The Nadir Crater offshore West Africa: a candidate cretaceous-paleogene impact structure. Sci. Adv. 8 (33), eabn3096. https://doi.org/10.1126/sciadv.abn3096.

Pasckert, J.H., Hiesinger, H., van der Bogert, C.H., 2018. Lunar farside volcanism in and around the South Pole–Aitken basin. Icarus 299, 538–562. https://doi.org/10.1016/j.icarus.2017.08.012.

Pierazzo, E., Melosh, H.J., 2000. Understanding oblique impacts from experiments, observations, and modeling. Annu. Rev. Earth Planet. Sci. 28 (1), 141–167. https://doi.org/10.1146/annurev.earth.28.1.141.

Quaide, W.L., Oberbeck, V.R., 1968. Thickness determinations of the lunar surface layer from lunar impact craters. J. Geophys. Res. 73 (16), 5247–5270. https://doi.org/10.1029/JB073i016p05247.

Racki, G., Koeberl, C., 2024. Impact catastrophism versus mass extinctions in retrospective, perspective and prospective: toward a phanerozoic impact event stratigraphy. Earth-Sci. Rev. 259, 104904. https://doi.org/10.1016/j.earscirev.2024.104904.

Stuart-Alexander, D.E., 1978. Geologic Map of the Central Far Side of the Moon. United States Geological Survey.

Wu, W., Li, C., Zuo, W., et al., 2019. Lunar farside to be explored by Chang'e-4. Nat. Geosci. 12 (4), 222–223. https://doi.org/10.1038/s41561-019-0341-7.

Yingst, R.A., Chuang, F.C., Berman, D.C., Mest, S.C., 2017. Geologic mapping of the Planck Quadrangle of the Moon (LQ-29). In: 48th Lunar and Planetary Science Conference, p. 1680.

Yuan, Y., Zhu, P., Xiao, L., 2021. Intermittent volcanic activity detected in the Von Kármán crater on the farside of the Moon. Earth Planet. Sci. Lett. 569, 117062. https://doi.org/10.1016/j.epsl.2021.117062.

Zhang, H., Zheng, L., Su, Y., et al., 2014. Performance evaluation of lunar penetrating radar onboard the rover of CE-3 probe based on results from ground experiments. Res. Astron. Astrophys. 14 (12), 1633. https://doi.org/10.1088/1674-4527/14/12/011.

Zhang, J., Zhou, B., Lin, Y., et al., 2021. Lunar regolith and substructure at Chang'E-4 landing site in South Pole–Aitken basin. Nat. Astron. 5 (1), 25–30. https://doi.org/10.1038/s41550-020-1197-x.

Zhang, L., Li, J., Zeng, Z., Xu, Y., Liu, C., Chen, S., 2020. Stratigraphy of the Von Kármán Crater based on Chang'E-4 lunar penetrating radar data. Geophys. Res. Lett. 47 (22), e2020GL088680. https://doi.org/10.1029/2020GL088680.

Zhang, L., Meng, X., Qian, Y., et al., 2025. A flat-bottomed buried crater and paleo-layered structures revealed at the Von Kármán Crater using Lunar Penetrating Radar. Astrophys. J. Lett. 978 (1), L2. https://doi.org/10.3847/2041-8213/ad1f1a.

Zhou, H., Feng, X., Ding, C., Dong, Z., Liu, C., Liang, W., 2022. Heterogeneous weathering process of lunar regolith revealed by polarimetric attributes analysis of Chang'E-4 Lunar Penetrating Radar data acquired during the Yutu-2 turnings. Geophys. Res. Lett. 49 (13), e2022GL099207. https://doi.org/10.1029/2022GL099207.